A finite element thermomechanical analysis of the development of wheel polygonal wear

He, Chunyan; Yang, Zhen; Zhang, Pan; Li, Shaoguang; Naeimi, Meysam; Dollevoet, Rolf; Li, Zili

DOI
10.1016/j.triboint.2024.109577

Publication date
2024

Document Version
Final published version

Published in
Tribology International

Tribology International 195 (2024) 109577

Contents lists available at ScienceDirect

Tribology International

journal homepage: www.elsevier.com/locate/triboint

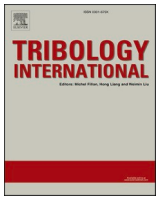

A finite element thermomechanical analysis of the development of wheel polygonal wear

Chunyan He, Zhen Yang *, Pan Zhang, Shaoguang Li, Meysam Naeimi, Rolf Dollevoet, Zili Li

Delft University of Technology, Section of Railway Engineering, Stevinweg 1, 2628 CN Delft, the Netherlands

ARTICLE INFO

Keywords:
Polygonal wear
Finite element model
Thermal effect
Wheel-rail contact

ABSTRACT

Polygonal wear is a type of damage commonly observed on the railway wheel tread. It induces wheel-rail impacts and consequent train/track components failure. This study presents a finite element (FE) thermomechanical wheel-rail contact model, which is able to cope with the three possible generation and development mechanisms of polygonal wear: initial defects, thermal effect, and structural dynamics. The polygonal wear-induced impact contact and further development of wear are simulated. The simulated elastic contact solutions are verified against the program CONTACT. Different material properties (elastic, elasto-plastic and elasto-plastic-thermo, i.e. with thermal softening) and initial polygonal profiles are then applied to the FE model to investigate the influence of wheel/rail material and wear amplitude on wheel-rail contact stress and wear development. The simulations indicate that the wheel-rail impact-induced temperature may reach up to 362 ℃ at the contact interface, and the high temperature at the contact area influences wheel-rail contact stress and wear depth.

1. Introduction

Polygonal wear is typical damage that occurs on the wheels of locomotives, metros, and high-speed trains [1–3]. High-amplitude vibrations induced by the impacts between rails and polygonal wheels accelerate train and track degradation and radiate high-level noises [4]. Severe polygonal wear threatens the safety of railway operations and adversely affects ride comfort of passengers [5]. To mitigate the effects of polygonal wear, a better understanding of its initiation and development mechanisms is needed.

The initiation and progression of polygonal wear on railway wheels can be influenced by three principal mechanisms, as identified in the previous research. Firstly, initial defects play a crucial role, arising from factors such as the wheel re-profiling process [6,7], uneven material properties [8], and static and dynamic imbalances [9]. Secondly, the natural vibrations within the train-track system may contribute to polygonal wear formation, driven by resonance frequencies from the vehicle components (e.g. wheelsets [10,11], bogie frames [3], and linear induction motors [12]), track components (e.g. rail bending vibration modes [13]), and train-track interactions including stick-slip oscillations [14], P2 resonance [15], and frictional self-excited vibrations [16]. Lastly, the thermal effect between the wheel tread and braking blocks [17,18] may further influence the development of polygonal wear.

Studies on the formation and growth of wheel polygonal wear have been conducted with numerical modeling. A general approach is to simulate wheel-rail contact and consequent wear by coupling a multi-body dynamics (MBD) model with a wear prediction model considering initial defects [19]. The initial wheel defects and wheel/rail structural dynamics, as possible mechanisms of wheel polygonal wear generation and development, can be considered in the MBD models. The initial polygonal wear profile of wheel could be simplified as one or several mixed harmonic waves. The number of waves along the wheel circumference is regarded as the 'order' of the polygonal wear. The core connections between a MBD model and a wear model are wheel-rail contact solutions, i.e. the normal and tangential contact stresses and micro-slip distributions.

Morys [20] built up a three-dimensional (3D) MBD model of an ICE-1 carriage. Hertzian theory and FASTISM [21] were used to calculate the normal and tangential contact solutions, respectively. The study presented the simulation results of the evolution of the worn profile, which was assumed to be proportional to the wear energy, and concluded that the low-order polygonal wear could be developed into higher-order harmonics. M. Meywerk [22] built up an MBD model with a wheelset, in which the wheel axle and rims were treated as flexible beams, and the bogie was simplified as a rigid frame. Kalker's linear theory [23] and Hertzian theory were employed to deal with the contact solutions. The

* Corresponding author.
E-mail address: Z.Yang-1@tudelft.nl (Z. Yang).

https://doi.org/10.1016/j.triboint.2024.109577
Received 27 January 2024; Received in revised form 10 March 2024; Accepted 20 March 2024
Available online 24 March 2024

study concluded that the phase shift of the left and right wheel profiles may influence the growth of polygonal wear, and the first and second bending modes of the wheelset axle are dominant contributors to polygonal wear growth. Andersson and Johanssons [15,24] developed a model incorporating multi-rigid body wheelsets and a bogie frame, as well as finite element rails. Hertzian theory and Shen-Hedrick-Elkins model [25] were employed to calculate contact solutions. They concluded that the P2 resonance could cause the 5th, 6th, and 7th-order polygonal wear, and the track modes are the main causes of the 14th to 20th-order polygonal wear. To deal with non-elliptical wheel-rail contact that occurs in the real-life operations [26], some MBD models applied non-Hertzian contact theories, e.g. ANALYN [27], modified Kik–Piotrowski [28] and FaStrip [29]. However, because wheel/rail material nonlinearities cannot be treated properly with the aforementioned contact methods, hardly can the MBD models accurately simulate polygonization-induced impact contact, where plasticity occurs, and be used to predict the further development of wear. To cope with the material nonlinearities, complex wheel-rail contact geometry, and dynamic effects involved in the wheel-rail interactions, explicit finite element (FE) contact modeling [30] has been broadly adopted to calculate wheel-rail dynamic contact, such as the polygonal wear-induced and flat-induced wheel dynamic responses [31,32]. However, few of them, if any, have been combined with wear models to analyze the initiation and further development of polygonal wear.

In addition, it has been found that the heat induced by wheel-rail frictional contact may significantly influence the material properties and consequently the evolution of wear [33]. Hence, friction-induced heat has been considered in some FE contact models. Asih [34] developed a two-dimensional (2D) FE model which applied an analytical moving heat flux on the rail to investigate the thermal effect on the wear rate of the rail. It was concluded that the transition from mild to server wear could happen when the temperature is above 350 °C. Wu et al. [35] built a 2D FE rail model and applied an instantaneous heat source to analyze the thermal effect on the rail. They concluded that the thermal effect influences the residual stress, deformation, and plastic strain of the rail. Vo et al. [36] compared the wheel-rail contact temperatures calculated with a 2D model and a 3D model, and found that the peak temperature on the rail calculated with the 2D model was overestimated because the thermal energy emission in the transverse direction was overlooked. Besides the limitation of the Hertzian elastic assumption used in the moving heat sources, all the studies above prescribed the thermal effect in the wheel-rail contact load. In other words, the thermal effect that should be influenced by frictional contact were not updated in the simulations. To obtain more accurate contact solutions with the consideration of thermal effect, Naeimi et al. [37] proposed a 3D dynamic FE wheel-rail contact model that couples the mechanical and thermal load to investigate the stress-strain responses and flash temperature on the rail surface. Considering the temperature-dependent nonlinear material properties, the temperature and stress field in the contact patch with a single wheel passage were obtained. The study concluded that the thermal softening of material induces higher von-Mises stresses and larger plastic deformation. The thermomechanical FE modeling approach proposed in [37] was then applied by Lian et al. [38] to study the fatigue life and wear behavior of a rail with multiple wheel loads. The thermomechanical FE model has been applied to study the stress and the flash temperature of the corrugated rail [39]. To the best of the authors' knowledge, an analysis of thermal effect on wheel polygonal wear has not been conducted.

In this study, a 3D FE thermomechanical wheel-rail contact model is presented to simulate polygonal wheel-rail interactions. The model is able to cope with the three possible generation and development mechanisms of polygonal wear: initial defects, thermal effect, and structural dynamics. In combination with Archard's wear model [40], the further development of wear is predicated. The FE model is built up based on the parameters of an in-house test rig—V-Track [41,42], to facilite the next-step model validation. Kalker's CONTACT program [43] is used to verify the elastic contact solutions obtained with the proposed FE model. Simulations using different wheel/rail material properties and initial wheel profiles are then conducted to investigate the influences of plasticity, the thermal effect, and initial defects on wheel-rail contact stress distributions and wear development.

2. Modeling

2.1. The FE thermomechanical model

Fig. 1 shows the 1/7 downscaled V-Track test rig and the FE thermomechanical wheel-rail contact model. The parameters used in the FE model are listed in Table 1. In the V-Track, the wheel assembly mounted on a steel frame can be powered by two motors and run along the ring track. One motor drives the steel frame together with the wheel assembly to run with a controllable translational velocity, and the other can provide a negative or positive torque to the rolling wheel to simulate a braking or traction loading condition. The V-Track has been proven to be able to reproduce real-life wheel-rail frictional rolling contact and to investigate the related problems [44,45]. In addition, the V-Track demonstrates notable dynamic similarity to real vehicle-track systems [46,47], which is important for the reproduction of wheel polygonal wear. Fig. 1(a) (and a close-up in Fig. 2) shows an example of wheel polygonal wear that was successfully produced in the V-Track test rig with the operational condition that the wheel speed was 13 km/h, and the wheel-rail normal, lateral and longitudinal contact forces were 4000 N (corresponding to the contact pressure of 1100 MPa), 80 N, and 1800 N, respectively.

In the FE model, the cylindrical wheel, rail, and sleepers are modeled with 8-node solid elements, as shown in Fig. 1(b). The fastenings and the ballast (physically modeled with clamps and rubber pads in V-Track) are modeled with spring-damper elements. The car body and bogie, which are physically modeled in V-Track with the steel frame, are simplified as lumped mass elements connected to the wheel axle with spring-damper elements which represent the primary suspension. The total length of the rail model is 3.07 m (with 24 sleeper spans) including a solution zone with a length of 0.17 m. To increase computation efficiency, a partially refined mesh strategy is applied. The solution zones on the wheel and rail have a fine mesh with a size of 0.14 mm (along the x-axis) $\times$ 0.20 mm (along the y-axis) $\times$ 0.20 mm (along the z-axis). The directions of the axis can be found in Fig. 1(b). The minor axis of the contact patch includes 20 elements along the running direction, which is sufficient for obtaining accurate contact solutions, as reported in [48].

An implicit-explicit sequential analysis is conducted to simulate wheel-rail frictional rolling contact. A static equilibrium of wheel loading on the rail is first performed in the commercial software ANSYS, in which the longitudinal and lateral degrees of freedom of the wheel axle are constrained. An explicit analysis is then conducted to simulate wheel rolling along the rail. The longitudinal constraint of the wheel axle is released in the explicit simulation. This study simulates wheel rolling with high longitudinal creepage, although high lateral creepage may contribute to the formation of polygonal wear [10,11,14] and can be simulated with the explicit FE analysis [49]. That is because this study aims to investigate the polygonal wear observed in the V-Track (shown in Fig. 1(a)), in the operational conditions of which the lateral creepage was controlled to a very small level, and the measured wheel-rail lateral contact force was only 1/22.5 of the longitudinal force. In the implicit-explicit sequential analysis, the nodal displacements obtained by the static equilibrium are taken as initial conditions for the explicit analysis. A positive torque is applied to the axle to simulate a driving wheel case. Three different types of materials, listed in Table 2, are applied to the wheel and rail models to investigate the influences of material plasticity and thermal effect on wheel-rail contact stress and wear development. The elasto-plastic material is simulated by a bilinear representation. The thermal softening is simulated by using temperature-dependent mechanical and thermal material parameters

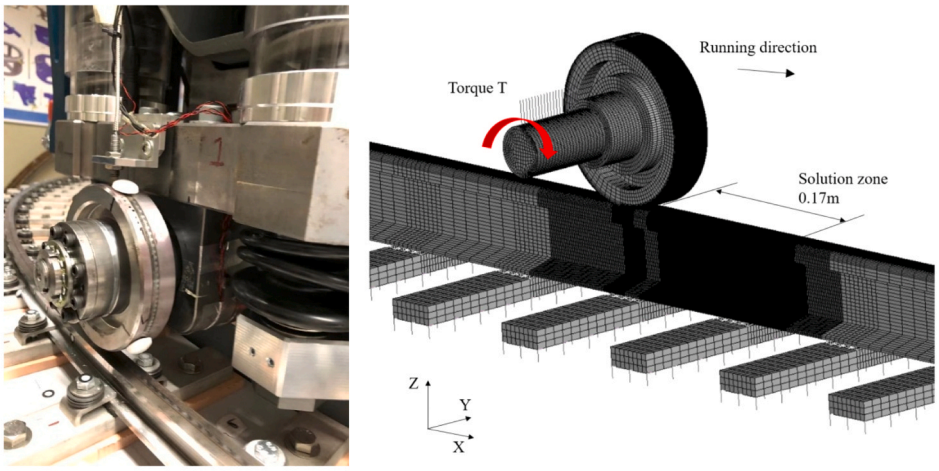

(a) A V-Track wheel with polygonal wear (b) The FE wheel-rail contact model

Fig. 1. The V-Track test rig and corresponding 3D FE thermomechanical wheel-rail contact model.

Table 1
Input parameters of the FE model.

Symbol (units)	Parameters	Value
ρ_0 (kg/m^3)	The density of wheel, rail, and sleeper material	7800
m (kg)	Total weight of the mass element	40
L (m)	The initial length of the primary suspension	0.0574
K_p (kN/m)	Stiffness of the primary suspension	11.5
C_p (N·s/m)	Damping of the primary suspension	5
K_f (kN/m)	Stiffness of the fastener	2220
C_f (N·s/m)	Damping of the fastener	21
K_b (kN/m)	Stiffness of the ballast	370
C_b (N·s/m)	Damping of the ballast	32
f	Coefficient of friction	0.45
R (mm)	Initial radius of the wheel	65
R' (mm)	Principal radii of rail	120
T_0 (℃)	Ambient temperature	25

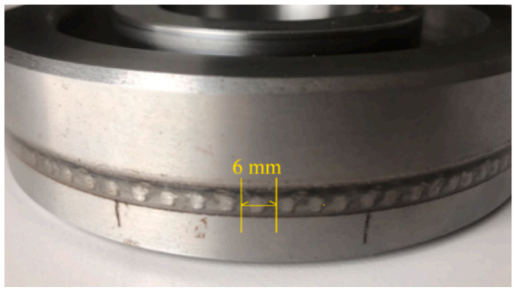

Fig. 2. Observed polygonal wear on a V-Track wheel with the cylindrical tread.

Table 2
The material models used in the simulations.

Material Type	Parameters	Value (unit)
Elastic	Young's modulus, E	210 (Gpa)
	Poisson's ratio, ν	0.3
Elasto-plastic	Young's modulus, E	210 (Gpa)
	Poisson's ratio, ν	0.3
	Yield stress, σ_y	483 (MPa)
	Tangent modulus, G	21 (Gpa)
Elasto-plastic-thermo with thermal softening	See the mechanical and thermal parameters in Tables 3 and 4	

Table 3
Temperature-dependent mechanical material parameters.

Temperature, T (℃)	Young's modulus, E (Gpa)	Poisson's ratio, ν	Yield stress, σ_y (MPa)	Coefficient of thermal expansion, α ($\times 10^{-6}$ ℃$^{-1}$)	Hardening modulus, E_p (Gpa)
24	213	0.295	483.0	9.89	22.7
230	201	0.307	485.1	10.82	26.9
358	193	0.314	418.8	11.15	21.3
452	172	0.320	332.4	11.27	15.6
567	102	0.326	151.1	11.31	6.2
704	50	0.334	45.0	11.28	1.0
900	43	0.345	13.4	11.25	0.1

Table 4
Temperature-dependent thermal material parameters.

Temperature, T (℃)	Specific heat capacity, c (J/kg℃)	Thermal conductivity, λ (W/m℃)
0	419.5	8.53
350	629.5	5.84
703	744.5	4.32
704	652.9	4.31
710	653.2	4.29
800	657.7	3.57
950	665.2	3.86
1200	677.3	4.35

listed in Tables 3 and 4, respectively.

The thermal conductivity is scaled by a factor of 1/7, according to the scaling strategy [50], to be consistent with the scale of V-Track. The calculations of the contact stress and friction-induced temperature rise (i.e. thermal effect) are coupled in the FE thermomechanical wheel-rail contact model [37].

2.2. Polygonal wheel profile

The polygonal worn profile applied to the wheel model is assumed as a harmonic wave given in Eq. (1):

$$R_p(\theta) = R + A\cdot\sin(N\cdot\theta)(0^\circ \le \theta \le 360^\circ) \quad (1)$$

where $R_p(\theta)$ is the varying radius of a polygonal wheel; R is the original radius of a round wheel; A is the amplitude of the polygonal wear; and N is the order number of the polygonal wear. $N = 68$ is used in this study,

corresponding to a wavelength of 6 mm, which is consistent with the observed wear wavelength of the V-Track wheel shown in Fig. 2. θ is the corresponding angle in the polar coordinate. In this study, θ also indicates the angular displacement of wheel rolling over the original position O, which increases from 0 to 90 degrees in the simulations, as shown schematically in Fig. 3.

2.3. Wear simulation

Archard's wear model has been proven to be reliable for wheel-rail contact-induced wear predictions [51,52]. It is employed in this study to predict wear development induced by polygonal wheel-rail impact, as given in Eq. (2):

$$\Delta r = k\frac{NS}{H} \tag{2}$$

where Δr is material loss depth, k is wear coefficient, N is normal contact stress between contact surfaces, S is relative sliding distance between two contact surfaces, and H is Vickers' hardness of the material. The wear coefficient k can be identified based on the coefficient map presented in [51], along with the contact load and relative sliding velocity calculated with the FE wheel-rail contact model. According to the wheel-rail contact simulation results (to be presented in Section 4), the wear coefficient k is taken as 10^{-3} which is based on the measurement of the wear depth of the wheel in Fig. 2. The Viker's hardness H is 261 MPa, which was measured via a hardness test on a V-Track wheel. The thermal effect and influence of plastic deformation on the hardness are ignored in the simulation. The wear depth of the wheel can thus be calculated using Eq. (2) at each time step based on the FE simulation results, i.e. micro-slip and the surface contact stress.

3. Model verification

Accurate calculations of contact are crucial for wear predictions. To verify the accuracy of the FE contact solutions obtained in this study, they are compared to the solutions calculated with the widely-accepted CONTACT program. Because CONTACT deals with steady-state elastic contact without the consideration of the thermal effect, the contact solutions obtained with the two elastic FE models (here named model E and model E-POL, for the ones with the round and polygonal wheel profiles, respectively) are compared to the CONTACT solutions in Sections 3.1 and 3.2. For model E-POL, the amplitude of the polygonal profile A is 0.029 mm, which equals to 1/7 (the scale of the V-Track) of the manufacturing tolerance of high-speed trains (where wheel polygons are commonly observed)—0.2 mm [6].

3.1. Elastic contact with a round wheel

A 87.75 N·m constant positive torque is first applied to model E, resulting in a traction coefficient of 0.27. A partial-slip contact case could then be simulated (considering the traction coefficient is smaller than the coefficient of friction 0.45 listed in Table 1), which is a critical characteristic of the frictional rolling contact [53]. Fig. 4(a), (b), and (c) show the comparisons between the FE contact solutions (model E at instant 9.84 ms) and CONTACT results in terms of the traction bound (i.e. the normal stress F_n times the coefficient of friction f), surface shear stress F_t, and micro-slip distributions. The slip and adhesion area within the contact patch can be distinguished by comparing the surface shear stress to the traction bound: the contact is in adhesion when the surface shear stress is blow the traction bound, and the contact is in slip when they are equal.

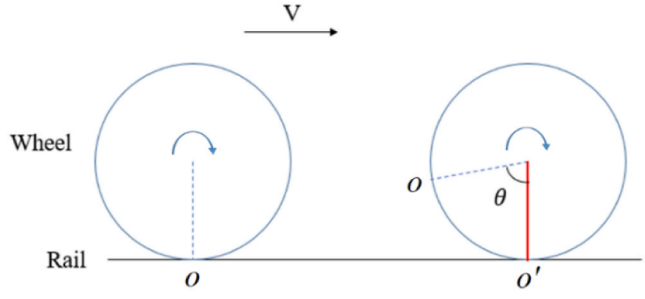

Fig. 3. The angular displacement that the wheel rolls over the rail in the simulation.

It could be seen that the contact stresses, i.e. the traction bound and surface shear stress, calculated with the FE model and CONTACT agree reasonably with each other. Differences are observed in the micro-slip calculations in the center line along the longitudinal axis ($y = 0$ mm) and in the vector graph within the contact patch, as shown in Fig. 4(b) and (c), respectively. The differences may result from the dynamic effects inherently involved in the FE modeling [48] but ignored in CONTACT. A better agreement can be achieved when the dynamic effects are mitigated in the FE modeling, e.g. by applying a gradually increased functional driving torque to facilitate the dynamic relaxation [54,55]. This study represents the torque applied to the FE model with a cosine function, as given in Eq. (3):

$$T(t) = \begin{cases} \dfrac{M}{2(1-\cos(\pi t/t_0)}, t < t_0 \\ M, t \geq t_0 \end{cases} \tag{3}$$

where T (t) is the time-dependent torque, t is the running time of the wheel, M is the maximum value of the torque, and t_0 is the duration required to reach M. The torque keeps constant after M is reached. Here, M= 87.75 N·m and t_0 = 2 ms. Fig. 4(d) and (e) show that when the functional torque is applied, the contact stresses and micro-slips at $y = 0$ mm calculated with the FE model and CONTACT have a better agreement. However, Fig. 4(c) and (f) show that in the FE contact solution, the micro-slips have more significant lateral components close to the top and bottom edges of the contact patch. To further mitigate the dynamic effects of the FE solutions, the Rayleigh damping coefficient used in the FE model is increased from 0.0001 to 0.1. Fig. 4(g), (h), and (i) compare the contact solutions obtained with the FE model E using the functional torque and a larger damping coefficient of 0.1 to those obtained with CONTACT. Excellent agreements are achieved, indicating that reliable contact solutions can be provided by the proposed FE model.

3.2. Elastic contact with a polygonal wheel

The radius of curvature of the wheel in the rolling direction, as a critical input for CONTACT, is adjusted to represent a polygonal wheel, which can be calculated with Eqs. (4) and (5) [56]:

$$k(\theta) = \frac{((x')^2 + (z')^2)^{3/2}}{|x'z'' - x''z'|} \tag{4}$$

$$\begin{cases} x = R_p(\theta)\cos(\theta) \\ z = R_p(\theta)\sin(\theta) \end{cases} \tag{5}$$

where $k(\theta)$ is the radius of curvature of the wheel in the rolling direction, and θ is the angular displacement of the wheel defined in Fig. 3. x and z represent the longitudinal and vertical coordinates of the node in the center line of the wheel tread ($y = 0$ mm) along the polygonal profile. x' and z' are the first-order derivatives. x'' and z'' are the second-order derivatives. The contact solutions calculated with the elastic polygonal wheel model, i.e. model E-POL, at 15 time steps (denoted as t1 to t15 in Fig. 5) are then analyzed in Figs. 6 and 7. Fig. 5 shows the wheel radial deviation from the original radius of a round wheel (i.e. the worn profile defined in Eq. (1)) as a function of angular displacement θ, which covers

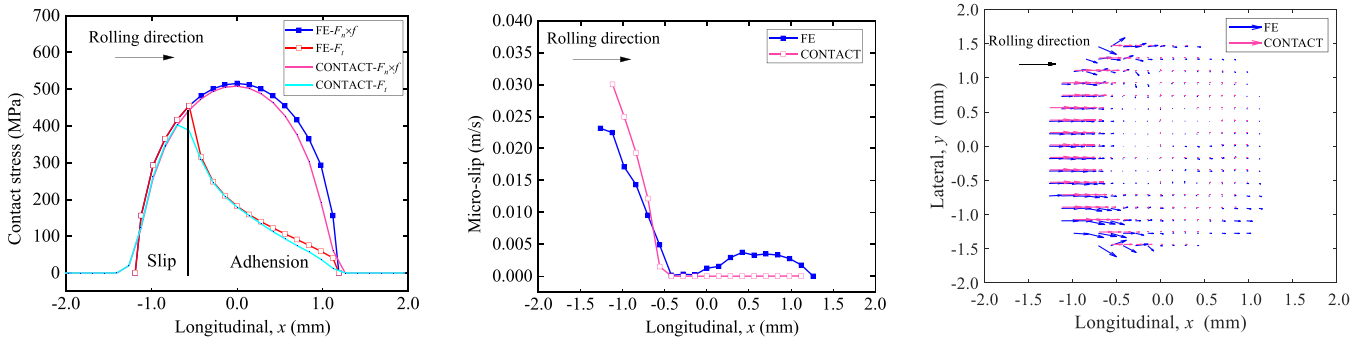

(a) Stress distribution with a constant torque and ξ=0.0001 (b) Micro-slip at y=0 mm with a constant torque and ξ=0.0001 (c) Micro-slip with a constant torque and ξ=0.0001

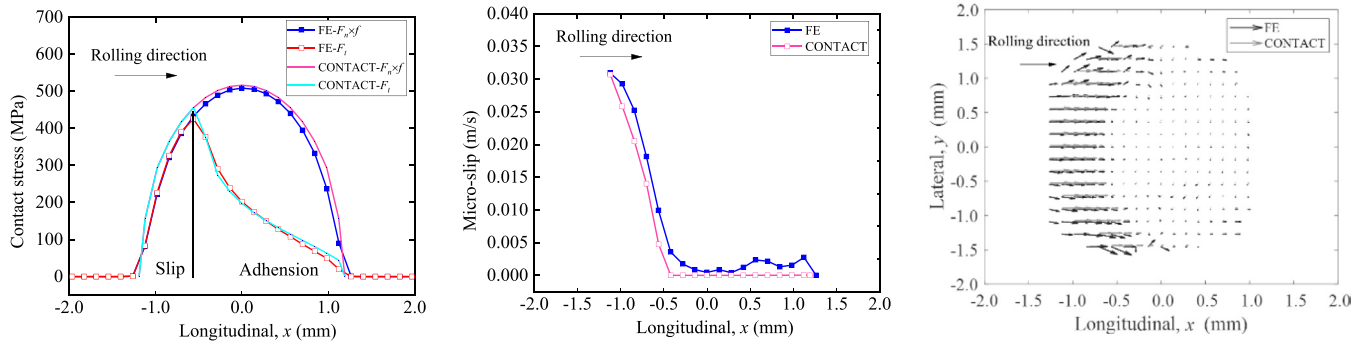

(d) Stress distribution with a functional torque (equation (3))and ξ=0.0001 (e) Micro-slip at y=0 mm with a functional torque and ξ=0.0001 (f) Micro-slip with a functional torque and ξ=0.0001

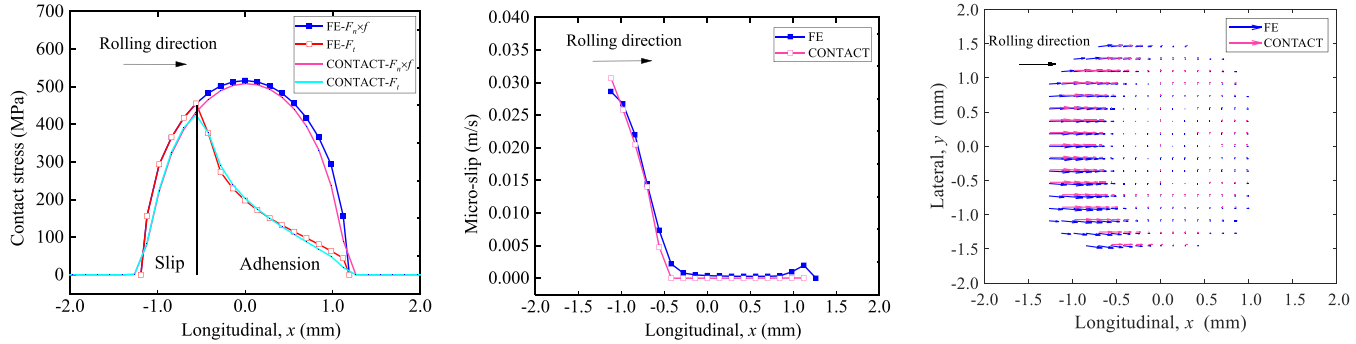

(g) Stress distribution with a functional torque and ξ=0.1 (h) Micro-slip at y=0 mm with a functional torque and ξ=0.1 (i) Micro-slip with a functional torque and ξ=0.1

Fig. 4. Comparisons between the contact solutions of the FE models and CONTACT program (The damping coefficient is denoted as ξ).

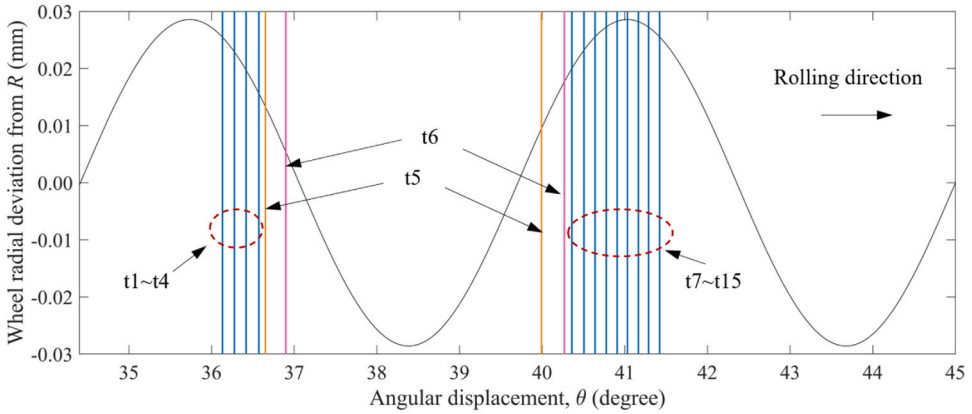

Fig. 5. The contact positions along the polygonal profile at 15 time steps.

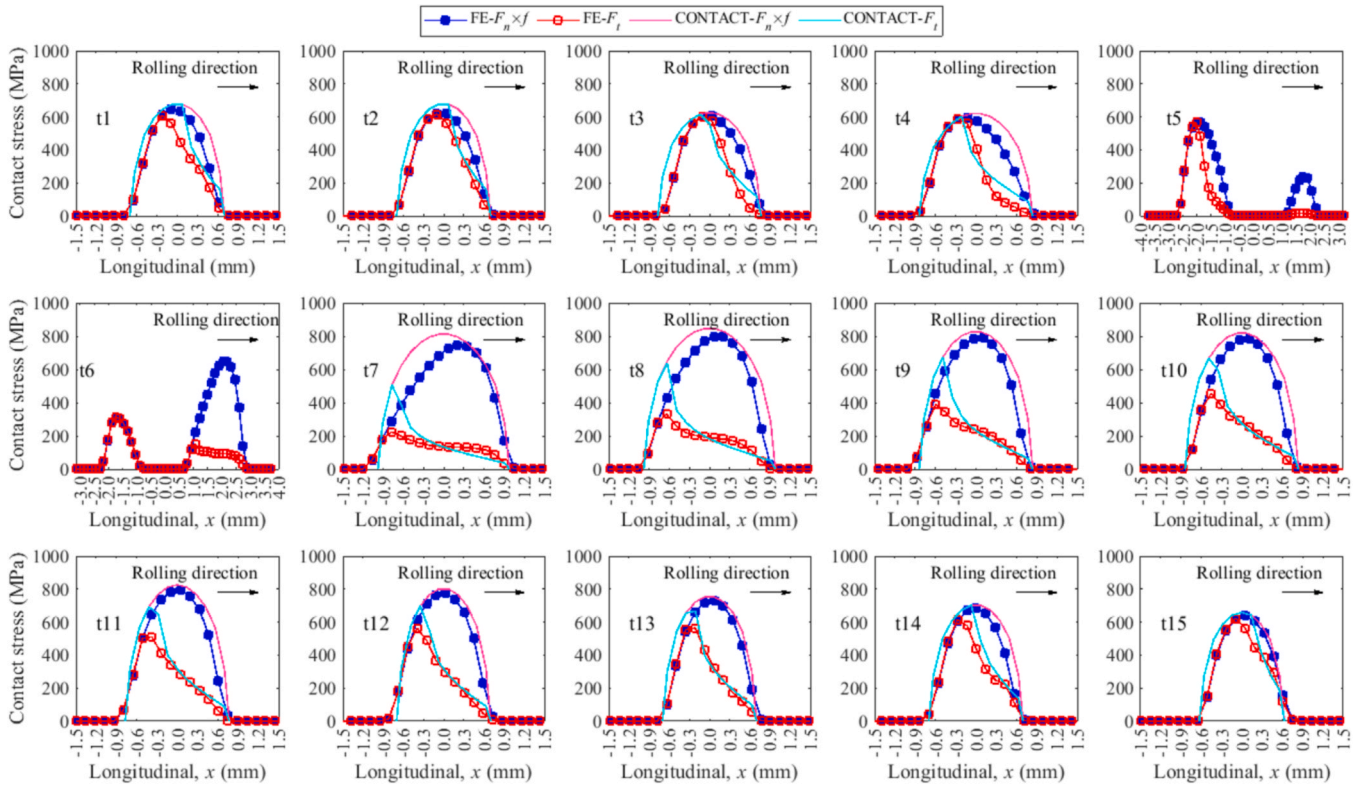

Fig. 6. Comparison between the contact stresses of the FE model E-POL and CONTACT.

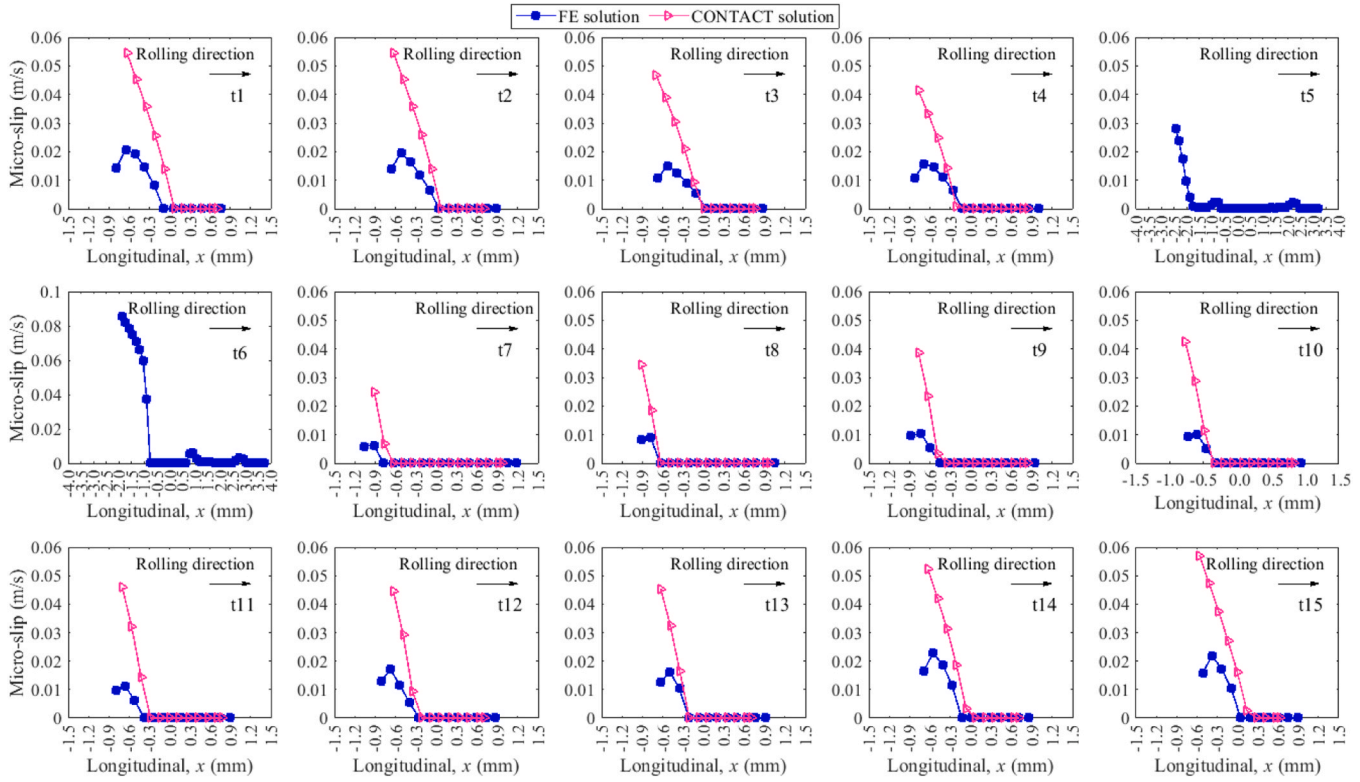

Fig. 7. Comparison between the micro-slip along the axis ($y = 0$ mm) of the FE model E-POL and CONTACT.

two wavelengths of the prescribed polygonal wear. 15 time steps with an interval of 0.12 ms are selected for the analysis to cover the wheel passage within one wavelength (between 36° and 41.5°). At t5 and t6, two-point wheel-rail contact occurs, and the corresponding contact positions along the wheel profile are indicated by the orange and pink vertical lines. Because prescribing the 4 principal radii for contact

geometry in CONTACT cannot deal with two-point contact, only the FE contact solutions at t5 and t6 are displayed in Figs. 6 and 7. The contact positions of the single-point contact cases (t1∼t4, and t7∼15) are indicated by blue vertical lines in Fig. 5.

It can be seen from Fig. 6, that the contact stress varies significantly from t1 to t15 with the change of the wheel contact radius. The proportion of the adhesion area increases slightly from t1 to t4. The surface stresses are not continuous at instants t5 and t6 due to the two-point contact. At instant t5, partial slip occurs in the 'left' contact patch, while the adhesion area occupies the whole 'right' contact patch. At instant t6, the 'left' contact patch is in slip, and partial slip occurs in the 'right' contact patch with a small proportion of slip area. A wheel-rail impact occurs after two-point contact, indicated by a significant increase in contact area as well as a high proportion of adhesion area at instants t7∼t8. A similar phenomenon has been observed when simulating a wheel-rail impact at an insulated rail joint [53]. The proportion of the adhesion area then decreases from t9 to t15 due to the rebound effect.

In Fig. 6, the traction bounds, especially the maximum normal contact stress, calculated with the FE model are generally in line with the results calculated with CONTACT, despite the presence of the polygonal profile. However, it is worth noticing that at t7 and t8 the peak normal contact stress moves forward to the leading side of the contact patch in the FE solutions due to impact, where the dynamic effects play an important role. The dynamic effects may also influence the maximum shear stress located at the border of the slip and adhesion regions: the FE solutions are lower from t7 to t15.

The corresponding micro-slip distributions along the longitudinal axis of the contact patch ($y = 0$ mm) calculated with the FE model and CONTACT are compared in Fig. 7. The peak values of the micro-slip calculated with CONTACT are higher than the FE solutions, similar to the case shown in Fig. 4(b). The difference in the calculated micro-slips is also believed to be attributed to the dynamic effect since it can be effectively mitigated by applying a functional torque, as shown in Fig. 4 (e) and (h). Here, in Fig. 7, although the functional torque has been applied in the FE simulation, the dynamic effect can still be remarkable because of the wheel polygonal profile and consequently the variation in contact geometry. The deviation in the micro-slip solutions suggests that the FE contact modeling with a better representation of dynamic contact should be applied to the polygonal wheel-rail impact contact study and further prediction of polygonal wear development.

4. Results and discussions

4.1. Simulation cases

Simulations using different wheel/rail material properties and wheel profiles are then conducted to investigate the influences of plasticity, thermal effect, and wheel polygonization on wheel-rail contact stress distributions and consequent wear development with a single wheel passage. Cyclic wheel loading, the accumulation of contact temperature, and their influences on polygonal wear growth can be analyzed using the explicit FE approach [57] in future research. Three different wheel/rail material properties (listed in Table 2) are applied to the FE models, as summarized in Table 5. Corresponding to the three material models, the FE wheel-rail contact models are named after E-POL, EP-POL, and EPT-POL, respectively. Note that model E-POL used here is the one used also in Section 3 but with a different setup of torque: a larger torque of 162.50 N·m is applied to model E-POL, as well as the other two models, in this section to achieve full slip wheel-rail contact. This is necessary for the examination of thermal effect, which plays a significant role when the wheel-rail slip ratio is high [37,38]. Three different amplitudes of polygonal profiles are then applied to model EP-POL and model EPT-POL, and the results are compared in Section 4.3 to examine the influence of initial defects on wear development.

Table 5
Simulation models with polygonal profile and different material properties.

Material type	Simulation models (abbreviation)	initial wear amplitude A (mm)
Elastic	E-POL	0.2
Elasto-plastic	EP-POL	0.1, 0.2, 0.3
Elasto-plastic-thermo with thermal softening	EPT-POL	0.1, 0.2, 0.3

4.2. Contact stress and wear

4.2.1. Results at one time step

Section 3 has demonstrated that the presented FE contact model is able to provide reliable elastic contact solutions for polygonal wear analysis. In this section, we first compare the normal contact stress and wear depth calculated with the three FE models listed in Table 5 at two different time steps (denoted as t1 and t2 in Fig. 10 and Fig. 11) because different wear phenomena are observed. The results are shown in Fig. 8 and Fig. 9, respectively. Because full slip wheel-rail contact is simulated, where the surface shear stress equals the traction bound and a constant coefficient of friction is used in this study, the distributions of the normal contact stress and shear stress follow the same pattern.

Fig. 8(a) shows that the normal contact stress obtained with the elastic model (i.e. model E-POL) is higher than those of the elasto-plastic models (i.e. model EP-POL and model EPT-POL), and the stress distributions are symmetrical in the elastic contact solutions, whereas the peak values shift forward in the elasto-plastic solutions. These correspond well to the results reported in [30,53]. The simulated flash temperature along the longitudinal centre line of the running band ($y = 0$ mm) is also displayed in Fig. 8(a), as denoted by the triangular markers. The temperature increases from the leading area to the trailing area, which is consistent with the result simulated in [58,59], because the cool materials enter the contact patch from the leading area and are heated up gradually due to the friction within the contact patch. In line with the results reported in [37], the peak normal contact stress simulated with model EPT-POL is higher than the pure mechanical solution obtained with model EP-POL due to the thermal softening and thermal expansion/contraction stress. At the central area of the contact patch (the longitudinal position x ranges from 0 to 0.5 mm, as denoted in Fig. 8), where the material yields due to high contact pressure and the flash temperature is around 150 ℃, the normal contact stress obtained with model EPT-POL is higher, partly because the hardening modulus and the coefficient of thermal expansion increase with temperature in the range between 24 ℃ and 230 ℃, as indicated in Table 3.

A similar trend can be seen in the wear depth results shown in Fig. 8 (b). According to Archard's wear model given in Eq. (2), wear depth is proportional to the normal contact stress when the wear coefficient is determined. In addition, the sliding distance, or the micro-slip in this case indicated by the pink curves (dotted, dashed and solid) in Fig. 8(b), contributes to the calculation of wear depth. We can see that the micro-slips of model E-POL and model EP-POL are close to each other, whereas the peak wear depth obtained with model E-POL is larger due to the higher normal contact stress. When the thermal softening is considered, the micro-slip is significantly increased (solid curve representing model EPT-POL). In combination with the increased normal contact stress shown in Fig. 8(a), the wear depth calculated with model EPT-POL is significantly larger than that obtained with the model EP-POL. This indicated that the maximum wheel-rail normal contact stress and wear are overestimated without considering material plasticity (E-POL vs EP-POL/EPT-POL), whereas they can be underestimated without considering thermal effects (EP-POL vs EPT-POL).

The results calculated at a later time step (i.e. instant t2) as shown in Fig. 9, present a more significant difference in the calculated normal contact stress obtained with model EP-POL and model EPT-POL. That is because the flash temperature at this step is higher, about 200 ℃ at the

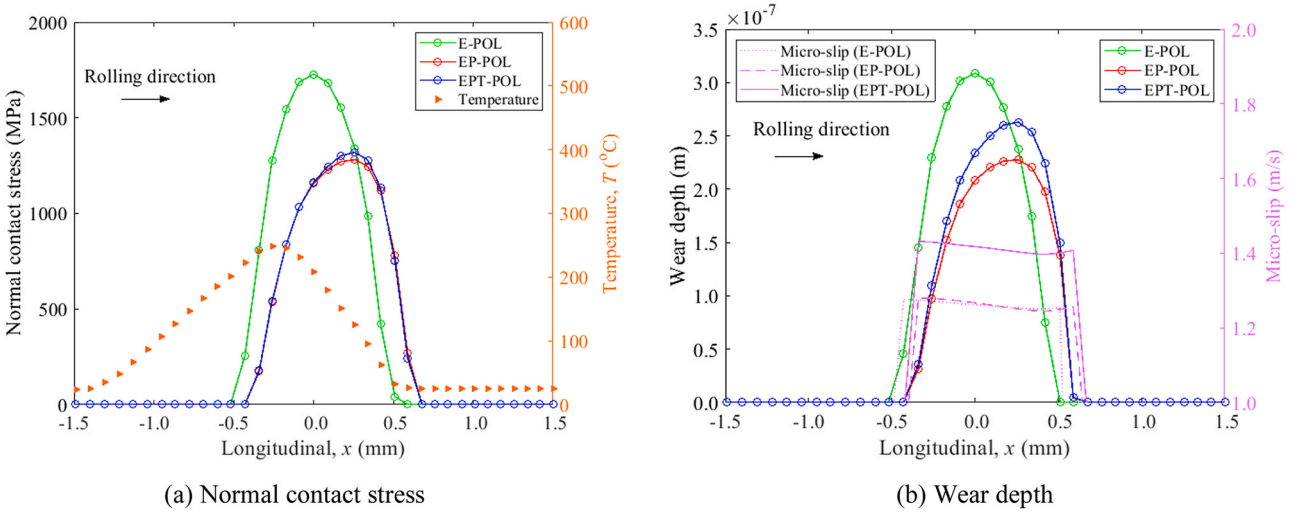

Fig. 8. Simulated normal contact stresses and wear depths in a single contact patch (at instant t1) using different material models.

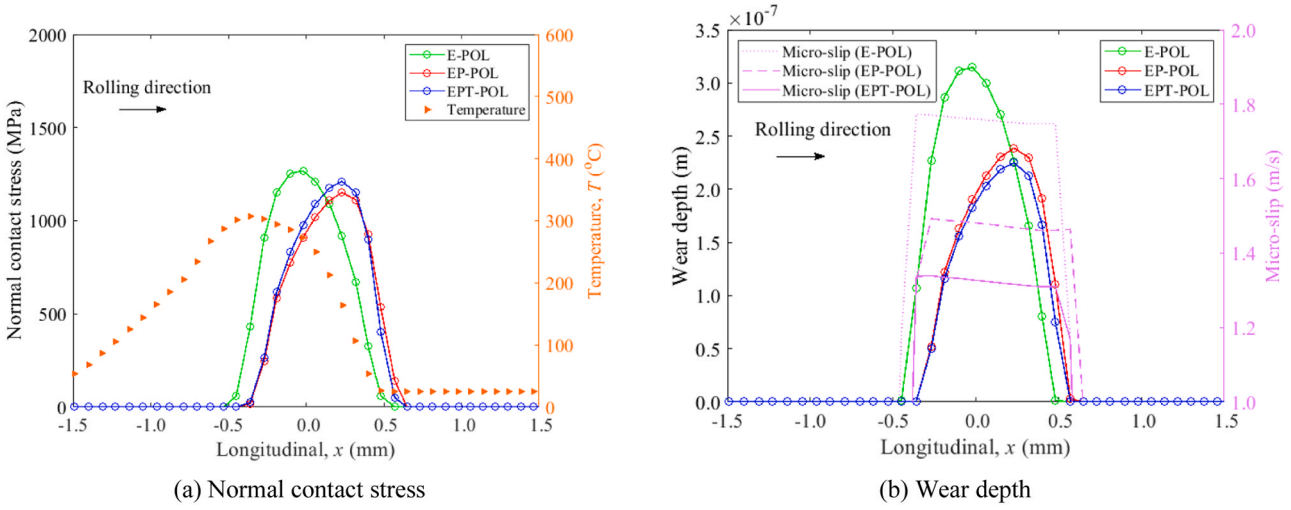

Fig. 9. Simulated normal contact stresses and wear depths in a contact patch (at instant t2) using different material models.

center of contact area. As to the results shown in Fig. 9(b), despite the smaller normal contact stress, the wear depth obtained with model EP-POL is greater than that of model EPT-POL, due to the remarkably larger micro-slip (dashed curve) than that of model EPT-POL (solid curve). This suggests that, again, the maximum wheel-rail normal contact stress is underestimated without considering thermal effects (EP-POL vs EPT-POL), whereas the wear depth can be either underestimated (Fig. 8 (b)) or overestimated (Fig. 9(b)), depending also on the value of micro-slip.

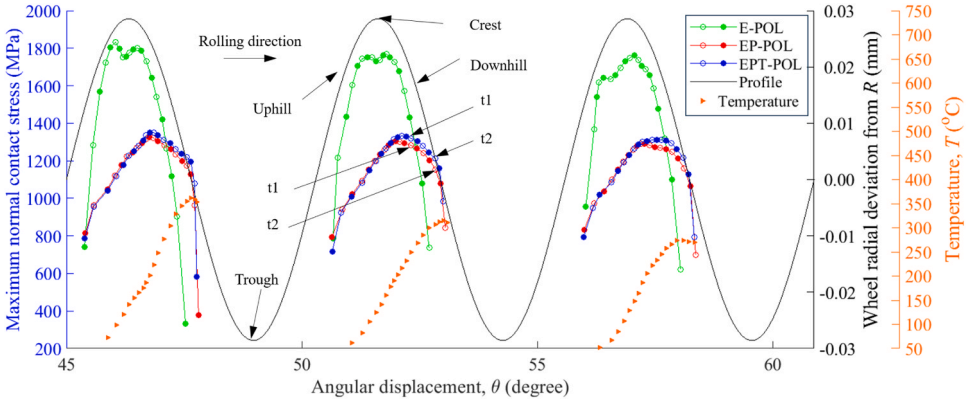

Fig. 10. The maximum normal contact stress and temperature in each contact patch along the wheel profile.

4.2.2. Results along the wheel profile

The analysis of results at one time step (Section 4.2.1) indicates the contact stress and wear depth may differ with time and slip ratio, the results along a section of wheel profile are thus analyzed in this section. In Fig. 10, the maximum normal contact stress calculated with the three models at a series of time steps (with an interval of 0.06 ms) are plotted as curves with markers against the polygonal wheel profile plotted as a solid curve. The markers indicate the peak values of the wheel-rail normal contact stress calculated at the time steps of concern. In order to visualize the results of different material models at the same time step, particularly the results obtained with model EP-POL and model EPT-POL, a series of curves characterized by an alternating pattern of solid and hollow dots has been plotted. For instance, the blue hollow dot and the red hollow dot below it represent the results of the same time step at t1 and t2. The lateral axis indicates the angular displacement that the wheel rolls over the rail, i.e. θ shown in Fig. 3, which covers three wavelengths of the polygonal profile. The maximum normal stress curves with markers are not continuous at the troughs of the wheel profile, because the troughs of wheel profile have no contact with rail, and two-point contact occurs at locations close to the trough, as presented in Section 3.2.

Along the wheel rolling direction, the area after the trough and before the next profile crest is identified as the 'uphill' area, whereas the 'downhill' area is located after the crest and before the next trough. In general, the normal contact stress increases along the 'uphill' profile and decreases along the 'downhill' profile with the variation of the wheel-rail contact geometry. This finding can be supported by [39], where a similar trend of the wheel-rail contact stress along the corrugated rail was presented. The difference between the elastic and elasto-plastic solutions are as follows: at most of the locations, the normal contact stresses calculated with the elastic model (E-POL) are higher than those calculated with the elasto-plastic models (EP-POL and EPT-POL), which is consistent with the one-time-step results presented in Section 4.2.1; the normal contact stress peaks of all the time steps obtained with the elasto-plastic models (EP-POL and EPT-POL) are not at the crest of the polygonal profile, but a bit forward at the 'downhill' area compared to the results calculated with model E-POL. That is because the maximum magnitude of the contact stress is located in the leading part of the wheel-rail contact patch when plastic deformation occurs [30,53].

To examine the effect of temperature, we may see again that the normal contact stress simulated with model EPT-POL is higher than the pure mechanical solution obtained with model EP-POL, also in line with the one-time-step results. Note that the difference occurs mainly at the 'downhill' area of the polygonal profile. This is because the temperature induced by wheel-rail contact at the 'downhill' area is higher. The simulated flash temperatures along the polygonal profile are also displayed in Fig. 10, as denoted by the orange triangular markers. The triangular maker shows the peak flash temperature within the contact patch at the corresponding time step. It can be seen that the temperature presents a periodic pattern along with the polygonal profile: the temperature is low at the locations just after the wheel profile trough, because of the two-point contact; and it goes up gradually and reaches the highest amplitude before decreasing slightly near the next trough. At the 'uphill' areas, the friction power which generates contact heat is lower because of the lower friction force (contact stress). It thus causes lower flash temperature. The heat is then accumulated with the increase of friction force, which causes the increase in temperature. When the contact position is at the 'downhill' area approaching the trough, the contact stress, and thus friction power (i.e. shear contact stress times micro-slip, which is not shown), decrease significantly (blue curve in Fig. 10), causing a reduction in the rate of temperature increase and the drop of contact temperature near the trough. While the friction power levels at certain positions at both the 'downhill' and 'uphill' areas are comparable, the temperature at the 'downhill' region is higher. This phenomenon can be attributed to the fact that contact temperature is influenced by both friction power and thermal conduction from adjacent positions [60,61]. The increased temperature of the wheel and rail at the 'downhill' area from the preceding time step rapidly propagates to the current materials in the contact patch, predominantly contributing to the higher contact temperature. The simulated peak contact temperature at the three waves of the analyzed polygonal profile are 362 ℃, 315 ℃, and 275 ℃, respectively. These simulation results agree reasonably with the experimental results obtained from an ongoing measurement conducted in the V-Track using an infrared camera. A comprehensive analysis of the measured results and the testing methodology will be presented in a follow-up paper.

The wear depths along the wheel polygonal profile simulated with the three models are compared in Fig. 11. The maximum wear depth calculated at the same time steps as those in Fig. 10 are plotted with a series of curves featuring an alternating pattern of solid and hollow dots markers against the polygonal profile of the wheel and the flash temperature. By comparing Fig. 10 to Fig. 11, an obvious difference can be noticed: the wear depth results have two peaks in each wavelength of the wheel polygonal profile, no matter what material is used. The formation of the two peaks could be related to the longitudinal compression mode of the V-Track rail with modal frequency of 2300~2700 Hz [62]. The wheel profile at the locations of the two peaks of wear depth may experience heavier material loss, and be developed into new troughs, as presented in [63]. The wear depth peaks calculated with the elastic model (E-POL) are significantly larger than those calculated with the elasto-plastic models (EP-POL and EPT-POL) due mainly to the higher contact stress. In addition, the positions of the two peaks and the dip calculated with the elasto-plastic models shift forward to the 'downhill' area in comparison with the results of elastic model. The dips between the two peaks of wear depth are located at the profile crest in the elastic simulation case, but a bit to the 'downhill' area in the elasto-plastic cases. This suggests that in the elastic contact case, the crests of the polygonal profile are less worn than the areas close by, and could thus be developed into higher-amplitude crests in the further cycles; and in the elasto-plastic case, the low-worn positions occur close to but after the crests of the polygonal profile.

By comparing the results of the two elasto-plastic models (EP-POL and EPT-POL), the thermal effect increases the 2nd peaks of wear depth, which are also located at the 'downhill' areas of the wheel polygonal profile where the simulated contact temperature is higher. The wear solutions presented in Figs. 8(b) and 9(b) correspond to the results at t1 and t2 in the second wave. It can thus be concluded that the thermal effect increases the wear depths of the 2nd peak at the 'downhill' area along the wheel profile, but the wear depth can be overestimated after the 2nd peak at the 'downhill' area without considering the thermal effect. The wear depth increased by the thermal effect of the 1st peak is not significant because lower contact temperature does not significantly influence the material properties. The thermal effect should be considered when a high contact temperature can be reached.

4.3. Influence of the initial wear amplitude

This section investigates the influence of initial defect amplitude on the development of polygonal wear. Three amplitudes of initial wheel polygonal profiles are applied to the elasto-plastic models (EP-POL and EPT-POL): A= 0.014 mm, 0.029 mm, and 0.043 mm (1/7 scaled down from 0.1 mm, 0.2 mm, and 0.3 mm), denoted by Profile-1, Profile-2 and Profile-3 in Fig. 12, respectively. Fig. 12 also displays the simulated wear depths along the prescribed initial profiles. In the legend, EP-POL-1 represents the wear depth simulated with model EP-POL with Profile-1, etc. We may see from Fig. 12 that the simulated wear depth peaks increase with the initial wear amplitude, suggesting that the development of polygonisation is an accelerating progress: the larger the polygonal wear, the faster the development is [63]. In addition, the 1st peak and 2nd peak of the wear depth move closer to the crest of the profile with the increase of initial wear amplitude, which indicates that locations at these peaks suffer from large-amplitude wear and result in

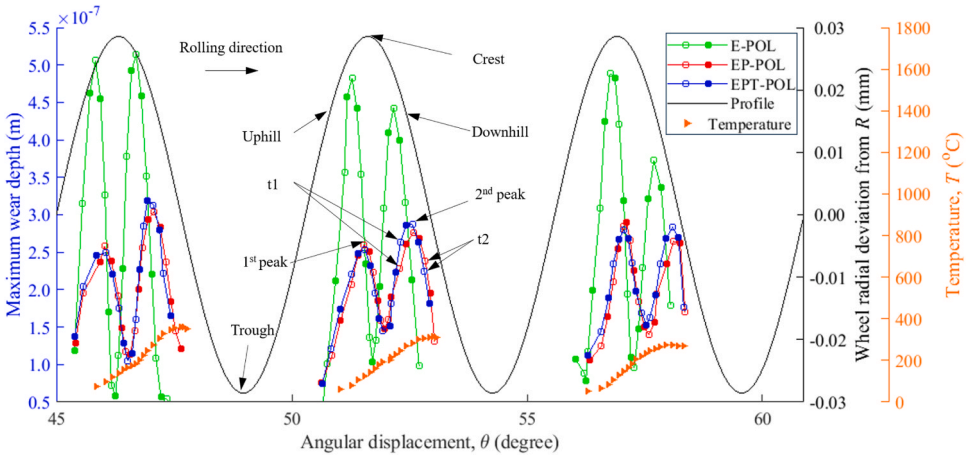

Fig. 11. The maximum wear depth and temperature in each contact patch along the wheel profile.

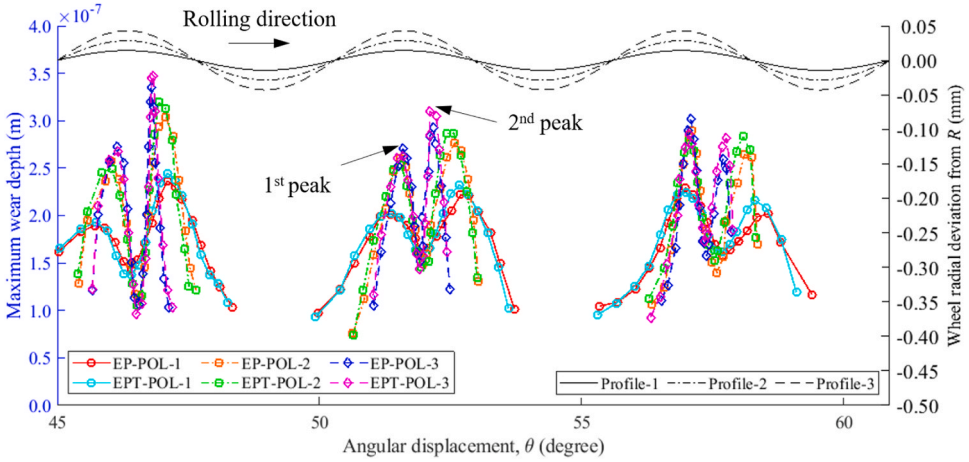

Fig. 12. Influence of the initial amplitudes on wear depth along the wheel profile.

the development of new polygonal profile. Furthermore, for all the simulation cases, the wear depth simulated with model EP-POL is smaller than that of model EPT-POL at the 2nd peak along the wheel profile where the wheel-rail contact-induced temperature is high.

5. Conclusions

To investigate the development of wheel polygonal wear, this study simulates impact contact between the polygonal wheel and rail using an FE thermomechanical analysis. The elastic contact solutions with a round and a polygonal wheel profile are verified against CONTACT program. The contact stress, temperature, and development of wheel polygonal wear are then investigated. Simulations with different materials (elastic, elasto-plastic and elasto-plastic-thermo, i.e. with thermal softening) and initial amplitudes are conducted to examine the influences of plasticity, thermal effect, and initial defects on the wheel-rail contact stress distributions and consequent wear development. The following conclusions can be drawn from this study:

1) The normal contact stress simulated with thermomechanical model is higher than the pure mechanical solution involving plasticity due to the thermal softening and thermal expansion/contraction stress, especially at locations after the crest of polygonal profile, where the contact temperature is high. The wheel-rail impact contact stress can thus be underestimated without considering thermal effects.
2) Within a contact patch, the contact temperature increases from the leading area to the trailing area, because cool materials enter the contact patch from the leading area and are then heated up during frictional rolling.
3) The contact temperature presents a periodic pattern along with the polygonal profile: the temperature is low at the locations just after the wheel profile trough and it goes up gradually and reaches the highest amplitude before decreasing slightly near the next trough. The simulated peak contact temperature at the three waves along the polygonal profile are 362 ℃, 315 ℃, and 275 ℃, respectively.
4) The material model influences wear depth calculation. The peaks of wear depth can be significantly overestimated when elastic model is used. The consideration of thermal effect increases the peaks of wear depth, especially when the contact temperature is high.
5) The simulated wear depth peaks increase with the initial polygonal wear amplitude, suggesting that with the increase of wear amplitudes, the development of polygonization is accelerated.

CRediT authorship contribution statement

Zhen Yang: Writing – review & editing. **Chunyan He:** Writing – original draft. **Shaoguang Li:** Software. **Pan Zhang:** Validation. **Meysam Naeimi:** Software. **Zili Li:** Supervision. **Rolf Dollevoet:** Supervision.

Declaration of Competing Interest

The authors declare the following financial interests/personal relationships which may be considered as potential competing interests: Chunyan He reports financial support was provided by the China Scholarship Council. If there are other authors, they declare that they have no known competing financial interests or personal relationships that could have appeared to influence the work reported in this paper.

Data Availability

Data will be made available on request.

Acknowledgements

This work was partly supported by the China Scholarship Council.

References

[1] Tao G, Wang L, Wen Z, Guan Q, Jin X. Experimental investigation into the mechanism of the polygonal wear of electric locomotive wheels. Veh Syst Dyn 2018;56:883–99. https://doi.org/10.1080/00423114.2017.1399210.
[2] Tao G, Wen Z, Liang X, Ren D, Jin X. An investigation into the mechanism of the out-of-round wheels of metro train and its mitigation measures. Veh Syst Dyn 2018;57:1–16. https://doi.org/10.1080/00423114.2018.1445269.
[3] Wu Y, Du X, Zhang H, Wen Z, Jin X. Experimental analysis of the mechanism of high-order polygonal wear of wheels of a high-speed train. J Zhejiang Univ-Sci A 2017;18:579–92. https://doi.org/10.1631/jzus.A1600741.
[4] Barke DW, Chiu WK. A review of the effects of out-of-round wheels on track and vehicle components. Proc Inst Mech Eng, Part F: J Rail Rapid Transit 2005;219:151–75. https://doi.org/10.1243/095440905x8853.
[5] Knothe K, Grassie S. Workshop on rail corrugations and out-of-round wheels. J Sound Vib 1999;227:895–7. https://doi.org/10.1006/jsvi.1999.2053.
[6] W. Rode, D. Müller, J. Villman, Results of DB AG investigations 'out-of-round wheels', Proceedings corrugation symposium–extended abstracts, IFV Bahntechink, 1997.
[7] Cui D, An B, Allen P, Wang R, Wang P, Wen Z, et al. Effect of the turning characteristics of underfloor wheel lathes on the evolution of wheel polygonisation. Proc Inst Mech Eng, Part F: J Rail Rapid Transit 2018;233:479–88. https://doi.org/10.1177/0954409718795760.
[8] Nielsen JCO, Johansson A. Out-of-round railway wheels-a literature survey. Proc Inst Mech Eng, Part F: J Rail Rapid Transit 2005;214:79–91. https://doi.org/10.1243/0954409001531351.
[9] Meinke P, Meinke S. Polygonalization of wheel treads caused by static and dynamic imbalances. Vibration 1999;227:979–86. https://doi.org/10.1006/jsvi.1999.2590.
[10] Jin X, Wu L, Fang J, Zhong S, Ling L. An investigation into the mechanism of the polygonal wear of metro train wheels and its effect on the dynamic behaviour of a wheel/rail system. Veh Syst Dyn 2012;50:1817–34. https://doi.org/10.1080/00423114.2012.695022.
[11] Tao G, Xie C, Wang H, Yang X, Ding C, Wen Z. An investigation into the mechanism of high-order polygonal wear of metro train wheels and its mitigation measures. Veh Syst Dyn 2020;59:1557–72. https://doi.org/10.1080/00423114.2020.1770810.
[12] Ma W, Song R, Luo S. Study on the mechanism of the formation of polygon-shaped wheels on subway vehicles. Proc Inst Mech Eng, Part F: J Rail Rapid Transit 2014;230:129–37. https://doi.org/10.1177/0954409714529269.
[13] Cai W, Chi M, Wu X, Li F, Wen Z, Liang S, et al. Experimental and numerical analysis of the polygonal wear of high-speed trains. Wear 2019;440:203079. https://doi.org/10.1016/j.wear.2019.203079.
[14] Kalousek J, Johnson K. An investigation of short pitch wheel and rail corrugations on the Vancouver mass transit system 1992;206:127–35. https://doi.org/10.1243/PIME_PROC_1992_206_226_02.
[15] Johansson A, Andersson C. Out-of-round railway wheels—a study of wheel polygonalization through simulation of three-dimensional wheel–rail interaction and wear. Veh Syst Dyn 2006;43:539–59. https://doi.org/10.1080/00423110500184649.
[16] Wu BW, Qiao QF, Chen GX, Lv JZ, Zhu Q, Zhao XN, et al. Effect of the unstable vibration of the disc brake system of high-speed trains on wheel polygonalization. Proc Inst Mech Eng, Part F: J Rail Rapid Transit 2019;234:80–95. https://doi.org/10.1177/0954409719833787.
[17] Vernersson T, Lundén R. Temperatures at railway tread braking. Part 3: wheel and block temperatures and the influence of rail chill. J Proc Inst Mech Eng, Part F: J Rail Rapid Transit 2007;221:443–54. https://doi.org/10.1243/09544097JRRT91.
[18] Vernersson T. Temperatures at railway tread braking. Part 1: modelling. J Proc Inst Mech Eng, Part F: J Rail Rapid Transit 2007;221:167–82. https://doi.org/10.1243/0954409JRRT57.
[19] Tao G, Wen Z, Jin X, Yang X. Polygonisation of railway wheels: a critical review. Railw Eng Sci 2020;28:317–45. https://doi.org/10.1007/s40534-020-00222-x.
[20] Morys B. Enlargement of out-of-round wheel profiles on high speed trains. J Sound Vib 1999;227:965–78. https://doi.org/10.1006/jsvi.1999.2055.
[21] Kalker JJ. A fast algorithm for the simplified theory of rolling contact. Veh Syst Dyn 2007;11:1–13. https://doi.org/10.1080/00423118208968684.
[22] Meywerk M. Polygonalization of railway wheels. Arch Appl Mech 1999;69:105–20. https://doi.org/10.1007/s004190050208.
[23] Kalker JJ. Survey of wheel—rail rolling contact theory. Veh Syst Dyn 2007;8:317–58. https://doi.org/10.1080/00423117908968610.
[24] Andersson C, Johansson A. Prediction of rail corrugation generated by three-dimensional wheel–rail interaction. Wear 2004;257:423–34. https://doi.org/10.1016/j.wear.2004.01.006.
[25] Shen Z, Hedrick J, Elkins J. A comparison of alternative creep force models for rail vehicle dynamic analysis. Veh Syst Dyn 2007;12:79–83. https://doi.org/10.1080/00423118308968725.
[26] Burgelman N, Sichani MS, Enblom R, Berg M, Li Z, Dollevoet R. Influence of wheel–rail contact modelling on vehicle dynamic simulation. Veh Syst Dyn 2015;53:1190–203. https://doi.org/10.1080/00423114.2015.1039550.
[27] Sh. Sichani M, Enblom R, Berg M. A novel method to model wheel–rail normal contact in vehicle dynamics simulation. Veh Syst Dyn 2014;52:1752–64. https://doi.org/10.1080/00423114.2014.961932.
[28] Sun Y, Zhai W, Guo Y. A robust non-Hertzian contact method for wheel–rail normal contact analysis. Veh Syst Dyn 2018;56:1899–921. https://doi.org/10.1080/00423114.2018.1439587.
[29] Sh. Sichani M, Enblom R, Berg M. An alternative to FASTSIM for tangential solution of the wheel–rail contact. Veh Syst Dyn 2016:748–64. https://doi.org/10.1080/00423114.2016.1156135.
[30] Zhao X, Li Z. A three-dimensional finite element solution of frictional wheel–rail rolling contact in elasto-plasticity. Proc Inst Mech Eng, Part J: J Eng Tribology 2015;229:86–100. https://doi.org/10.1177/1350650114543717.
[31] Liu K, Jing L. A finite element analysis-based study on the dynamic wheel–rail contact behaviour caused by wheel polygonization. Proc Inst Mech Eng, Part F: J Rail Rapid Transit 2020;234:1285–98. https://doi.org/10.1177/0954409719891549.
[32] Han L, Jing L, Liu K. A dynamic simulation of the wheel–rail impact caused by a wheel flat using a 3-D rolling contact model. J Mod Transp 2017;25:124–31. https://doi.org/10.1007/s40534-017-0131-0.
[33] Lewis R, Olofsson U. Mapping rail wear regimes and transitions. Wear 2004;257:721–9. https://doi.org/10.1016/j.wear.2004.03.019.
[34] Asih AMS, Ding K, Kapoor A. Modelling rail wear transition and mechanism due to frictional heating. Wear 2012;284-285:82–90. https://doi.org/10.1016/j.wear.2012.02.017.
[35] Wu L, Wen Z, Li W, Jin X. Thermo-elastic–plastic finite element analysis of wheel/rail sliding contact. Wear 2011;271:437–43. https://doi.org/10.1016/j.wear.2010.10.034.
[36] Vo K, Tieu AK, Zhu H, Kosasih P. The influence of high temperature due to high adhesion condition on rail damage. Wear 2015;330:571–80. https://doi.org/10.1016/j.wear.2015.01.059.
[37] Naeimi M, Li S, Li Z, Wu J, Petrov RH, Sietsma J, et al. Thermomechanical analysis of the wheel-rail contact using a coupled modelling procedure. Tribology Int 2018;117:250–60. https://doi.org/10.1016/j.triboint.2017.09.010.
[38] Lian Q, Deng G, Tieu AK, Li H, Liu Z, Wang X, et al. Thermo-mechanical coupled finite element analysis of rolling contact fatigue and wear properties of a rail steel under different slip ratios. Tribology Int 2020;141:105943. https://doi.org/10.1016/j.triboint.2019.105943.
[39] Chen YC, Lee SY. Elastic-plastic wheel-rail thermal contact on corrugated rails during wheel braking. J Tribology 2009;131. https://doi.org/10.1115/1.2991163.
[40] Archard J, Hirst W. The wear of metals under unlubricated conditions. Proc R Soc Lond Ser A Math Phys Sci 1956;vol. 236:397–410. https://doi.org/10.1098/rspa.1956.0144.
[41] Naeimi M, Li Z, Petrov RH, Sietsma J, Dollevoet R. Development of a new downscale setup for wheel-rail contact experiments under impact loading conditions. Exp Tech 2018;42:1–17. https://doi.org/10.1007/s40799-017-0216-z.
[42] Zhang P, Moraal J, Li Z. Design, calibration and validation of a wheel-rail contact force measurement system in V-Track. Measurement 2021;175:109105. https://doi.org/10.1016/j.measurement.2021.109105.
[43] Kalker JJ. Three-dimensional elastic bodies in rolling contact. Springe Sci Bus Media 2013;Vol. 2.
[44] Yang Z, Zhang P, Moraal J, Li Z. An experimental study on the effects of friction modifiers on wheel–rail dynamic interactions with various angles of attack. Railw Eng Sci 2022;30:360–82. https://doi.org/10.1007/s40534-022-00285-y.
[45] Zhang P, Li Z. Experimental study on the development mechanism of short pitch corrugation using a downscale V-Track test rig. Tribology Int 2023;180. https://doi.org/10.1016/j.triboint.2023.108293.
[46] Shen C, Dollevoet R, Li Z. Fast and robust identification of railway track stiffness from simple field measurement. Mech Syst Signal Process 2021;152. https://doi.org/10.1016/j.ymssp.2020.107431.
[47] M. Molodova, Detection of early squats by axle box acceleration, Delft University of Technology, The Netherlands, 2013. PhD Thesis.
[48] Zhao X, Li Z. The solution of frictional wheel–rail rolling contact with a 3D transient finite element model: validation and error analysis. Wear 2011;271:444–52. https://doi.org/10.1016/j.wear.2010.10.007.
[49] Yang Z, Li Z. Numerical modeling of wheel-rail squeal-exciting contact. Int J Mech Sci 2019;153-154:490–9. https://doi.org/10.1016/j.ijmecsci.2019.02.012.
[50] Jaschinski A, Chollet H, Iwnicki S, Wickens A, Von Würzen J. The application of roller rigs to railway vehicle dynamics. Veh Syst Dyn 1999;31:345–92. https://doi.org/10.1076/vesd.31.5.345.8360.
[51] Jendel T. Prediction of wheel profile wear—comparisons with field measurements. Wear 2002;253:89–99. https://doi.org/10.1016/S0043-1648(02)00087-X.

[52] Brouzoulis J, Torstensson PT, Stock R, Ekh M. Prediction of wear and plastic flow in rails—test rig results, model calibration and numerical prediction. Wear 2011; 271:92–9. https://doi.org/10.1016/j.wear.2010.10.021.
[53] Yang Z, Boogaard A, Wei Z, Liu J, Dollevoet R, Li Z. Numerical study of wheel-rail impact contact solutions at an insulated rail joint. Int J Mech Sci 2018;138:310–22. https://doi.org/10.1016/j.ijmecsci.2018.02.025.
[54] Yang Z, Deng X, Li Z. Numerical modeling of dynamic frictional rolling contact with an explicit finite element method. Tribology Int 2019;129:214–31. https://doi.org/10.1016/j.triboint.2018.08.028.
[55] Wei Z, Li Z, Qian Z, Chen R, Dollevoet R. 3D FE modelling and validation of frictional contact with partial slip in compression–shift–rolling evolution. Int J Rail Transp 2015;4:20–36. https://doi.org/10.1080/23248378.2015.1094753.
[56] Do Carmo MP. Differential geometry of curves and surfaces: revised and updated second edition. Courier Dover Publications; 2016.
[57] Li S, Naeimi M, He C, Dollevoet R, Li Z. An integrated 3D dynamic FE vehicle-track model in elasto-plasticity to investigate short pitch corrugation under cyclic wheel loads. Structures 2023;53:1000–11. https://doi.org/10.1016/j.istruc.2023.05.001.
[58] Knothe K, Liebelt S. Determination of temperatures for sliding contact with applications for wheel-rail systems. Wear 1995;189:91–9. https://doi.org/10.1016/0043-1648(95)06666-7.
[59] Oestringer LJ, Proppe C. On the transient thermomechanical contact simulation for two sliding bodies with rough surfaces and dry friction. Tribology Int 2022;170. https://doi.org/10.1016/j.triboint.2021.107425.
[60] John OH. LS-DYNA theory manual. California: Livermore Software Technology Corporation; 2006.
[61] Necati OM. Heat conduction. John Wiley & Sons, Inc; 1993.
[62] Zhang P, He C, Shen C, Dollevoet R, Li Z. Comprehensive validation of three-dimensional finite element modelling of wheel-rail high-frequency interaction via the V-Track test rig. Veh Syst Dyn 2024:1–25. https://doi.org/10.1080/00423114.2024.2304626.
[63] Fu B, Bruni S, Luo S. Study on wheel polygonization of a metro vehicle based on polygonal wear simulation. Wear 2019;438-439. https://doi.org/10.1016/j.wear.2019.203071.